Encoding and Decoding with Prior Knowledge: From SLIM to SPICE

Chao Ma, Fan Lam & Zhi-Pei Liang

University of Illinois at Urbana-Champaign, Champaign, IL, USA

Conventional magnetic resonance spectroscopic imaging (MRSI) is a Fourier transform-based imaging technique. During data acquisition, Fourier encodings or (k, t)-space data are acquired. Decoding (or image reconstruction) is often accomplished using the truncated Fourier series. To overcome the well-known limited-data problem with Fourier transform MRSI, several constrained MRSI methods have been developed to exploit prior knowledge to improve the coding (data acquisition) and decoding (image reconstruction) process. This article reviews two of these constrained MRSI methods: SLIM (Spectral Localization by IMaging) and SPICE (SPectroscopic Imaging by exploiting spatiospectral CorrElation). SLIM is a classical method designed to use explicit boundary information obtained from anatomical imaging to improve spectral localization; SPICE is a modern method that exploits the subspace (or low-rank) structure of spatiospectral functions for efficient spatiospectral encoding and high-quality image reconstruction from sparsely sampled data.

Keywords: Nyquist criterion, Gibbs artifact, constrained reconstruction, sparse sampling, partial separability, low-rank model, subspace model

How to cite this article:
eMagRes, 2015, Vol 4: 535–542. DOI 10.1002/9780470034590.emrstm1441

Introduction

Magnetic resonance spectroscopic imaging (MRSI) is a Fourier transform-based imaging technique. During data acquisition, Fourier encodings or (k, t)-space data are acquired, which can be expressed as

$$s(\mathbf{k},t) = \int_{\mathcal{D}}\int_{\Omega_f} \rho(\mathbf{r},f)\mathrm{e}^{-i2\pi ft}\mathrm{e}^{-i\gamma\Delta B_0(\mathbf{r})t}\mathrm{e}^{-i2\pi\mathbf{k}\cdot\mathbf{r}}df d\mathbf{r} + \xi(\mathbf{k},t)$$
$$= \int_{\mathcal{D}} \tilde{\rho}(\mathbf{r},t)\mathrm{e}^{-i\gamma\Delta B_0(\mathbf{r})t}\mathrm{e}^{-i2\pi\mathbf{k}\cdot\mathbf{r}}d\mathbf{r} + \xi(\mathbf{k},t) \quad (1)$$

where $\rho(\mathbf{r},f)$ is the desired spatiospectral function, $\mathcal{D}$ the excited volume of interest, Ω_f the desired spectral bandwidth, γ the gyromagnetic ratio, $\Delta B_0(\mathbf{r})$ the B_0 field inhomogeneity map, and $\xi(\mathbf{k},t)$ the measurement noise (often assumed to be white Gaussian).

Conventional MRSI methods (most notably, the chemical shift imaging (CSI) technique[1]) sample the (k, t)-space uniformly at the Nyquist rate and reconstruct the underlying spatiospectral function from the measured data using Fourier transform-based methods. The only prior information used in the data acquisition (encoding) and image reconstruction (decoding) process of these methods is that the spatiospectral functions have limited spatial support (field-of-view, FOV) and spectral bandwidth. While these methods are very easy to use, they suffer from several well-known limitations, including long-data acquisition time, poor spatial resolution, and low signal-to-noise ratio (SNR). To speed-up data acquisition, many fast-scan methods (and pulse sequences) have been proposed (a comprehensive review can be found in Ref. 2). Although these methods can greatly reduce the data acquisition time for spatiospectral encoding, they sacrifice the already low SNR, which can be a significant problem for in vivo MRSI experiments. Figure 1 shows a set of MRSI results to illustrate the limitations with CSI and echo-planar spectroscopic imaging (EPSI)[3] (see ***Chemical Shift Imaging*** and ***High-speed MRS with PEPSI and spiral MRS***). We next discuss the use of prior knowledge to improve MRSI through two specific examples: Spectral Localization by IMaging (SLIM)[4] and SPectroscopic Imaging by exploiting spatiospectral CorrElation (SPICE).[5] SLIM is a classical method designed to use explicit boundary information obtained from anatomical imaging to improve spectral localization; SPICE is a modern method that exploits the subspace (or low-rank) structure of spatiospectral functions for efficient spatiospectral encoding and high-quality image reconstruction from sparsely sampled data. Both are described in detail subsequently.

SLIM: Spectral Localization with Boundary Constraints

The SLIM technique is motivated by the fact that in biological systems, the water proton distribution is closely related to the distributions of other metabolites of interest. Particularly, the boundaries of the body, organs, tissue types, or lesions revealed by high-resolution anatomical imaging often

© 2015 John Wiley & Sons, Ltd.

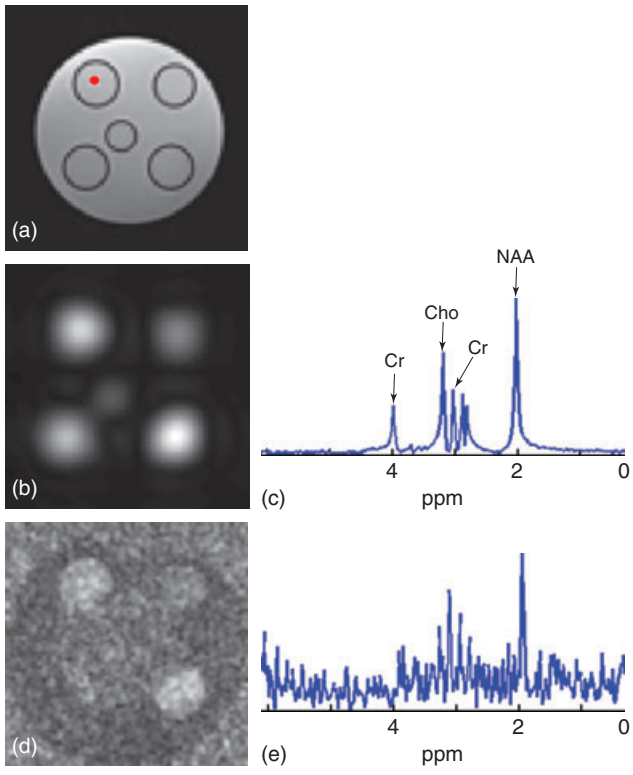

Figure 1. CSI and EPSI results from a metabolite phantom. (a) Structural reference image. (b) and (c) NAA map and representative spectrum [from the marked pixel in (a)] reconstructed from a CSI dataset with 19 × 19 spatial encodings and 2000 Hz readout bandwidth. (d) and (e) NAA map and representative spectrum reconstructed from an EPSI dataset with 100 × 100 spatial encodings, 167 kHz readout bandwidth, and two signal averages. The labeled peaks are due to N-acetylaspartate (NAA), creatine (Cr), and choline-containing compounds (Cho). The data acquisition time for both the CSI and EPSI scans was 6 min. As can be seen, the CSI reconstruction has high SNR but suffers from significant blurring artifacts because of limited k-space coverage; the EPSI reconstruction has high resolution but suffers from very low SNR because of the small voxel size and the high readout bandwidth

represent metabolic concentration discontinuities. SLIM is one of the earliest constrained MRSI methods that incorporate anatomical boundary constraints into the reconstruction of the spatiospectral function $\rho(\mathbf{r}, f)$.

Method

In SLIM, the anatomical image is used to define a set of generalized voxels $\mathcal{D}_m$, called *compartments*, with arbitrary shapes and sizes to match exactly the biological regions of interest and the objective is to reconstruct the average spectral distribution of each individual compartment using only a small number of encodings.

In a mathematical sense, for an M-compartment model, the SLIM spectral function is given by

$$\rho_{\text{slim}}(\mathbf{r}, f) = \sum_{m=1}^{M} \hat{\rho}_m(f), \tag{2}$$

where $\hat{\rho}_m(f)$ is an estimate of the desired average compartmental spectrum $\rho_m(f)$, namely,

$$\hat{\rho}_m(f) \approx \rho_m(f) = \begin{cases} \frac{1}{V_m}\int_{\mathcal{D}_m} \rho(\mathbf{r}, f)d\mathbf{r}, & \text{for } \mathbf{r} \in \mathcal{D}_m, \\ 0, & \text{otherwise}, \end{cases} \tag{3}$$

in which $\mathcal{D}_m$ is the compartmental geometry defined from the corresponding anatomical image and V_m is the volume of $\mathcal{D}_m$.

With the SLIM model in equations (2) and (3), the spectral reconstruction problem reduces to finding the compartmental spectrum $\hat{\rho}_m(f)$, which can be determined by solving the following least-squares problem[4]:

$$\min_{\{\hat{\rho}_m(f)\}_{m=1}^{M}} \sum_{n=1}^{N} \left| s(\mathbf{k}_n, t) - \int_{\mathcal{D}} \left[\sum_{m=1}^{M} \int_{-\infty}^{\infty} \hat{\rho}_m(f) \mathrm{e}^{-i2\pi ft} df \right] \mathrm{e}^{-i2\pi \mathbf{k}_n \cdot \mathbf{r}} d\mathbf{r} \right|^2, \tag{4}$$

where N is the total number of Fourier encoding steps. In this way, the boundary information is explicitly enforced into the reconstruction for improved localization. Ignoring temporarily measurement noise and compartmental inhomogeneities, one obtains

$$\begin{bmatrix} g_{11} & g_{12} & \cdots & g_{1M} \\ g_{21} & g_{22} & \cdots & g_{2M} \\ \vdots & \vdots & \ddots & \vdots \\ g_{N1} & g_{N2} & \cdots & g_{NM} \end{bmatrix} \begin{bmatrix} c_{\text{slim},1}(t) \\ c_{\text{slim},2}(t) \\ \vdots \\ c_{\text{slim},M}(t) \end{bmatrix} = \begin{bmatrix} s(\mathbf{k}_1, t) \\ s(\mathbf{k}_2, t) \\ \vdots \\ s(\mathbf{k}_N, t) \end{bmatrix}, \tag{5}$$

where g_{nm} is the phase dispersal factor of the nth phase-encoding wave vector across the mth compartment,

$$g_{nm} = \int_{\mathcal{D}_m} \mathrm{e}^{-i2\pi \mathbf{k}_n \cdot \mathbf{r}} d\mathbf{r}, \tag{6}$$

and $c_{\text{slim},m}(t)$ is the compartmental spectroscopic signal related to $\hat{\rho}_m(f)$ by

$$c_{\text{slim},m}(t) = \int_{-\infty}^{\infty} \hat{\rho}_m(f) \mathrm{e}^{-i2\pi ft} df. \tag{7}$$

In vector notation, equation (5) can be written as

$$\mathbf{G}\mathbf{c}_{\text{slim}}(t) = \mathbf{s}(t), \tag{8}$$

where $\mathbf{G}$ is called the *SLIM geometry matrix*, and the least-squares solution for $\mathbf{c}_{\text{slim}}(t)$ is given by

$$\mathbf{c}_{\text{slim}}(t) = (\mathbf{G}^{\text{H}}\mathbf{G})^{-1}\mathbf{G}^{\text{H}}\mathbf{s}(t) = \mathbf{G}^{+}\mathbf{s}(t). \tag{9}$$

The entire processing pipeline for SLIM is summarized in the flow chart in Figure 2.

© 2015 John Wiley & Sons, Ltd.

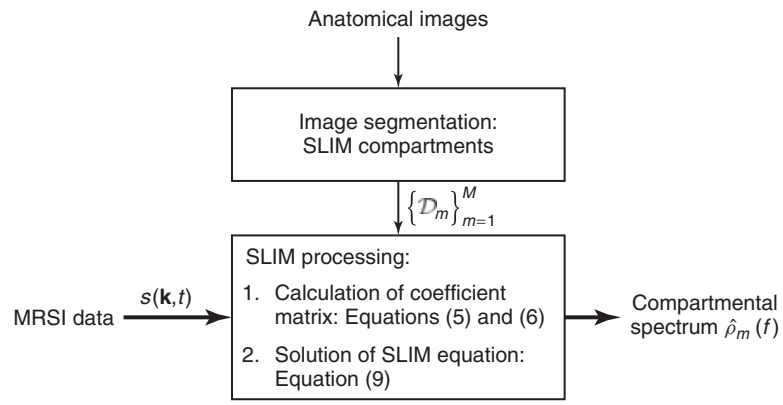

Figure 2. SLIM processing flow chart

Effects of Measurement Noise

In practical applications, random measurement noise is always present. Incorporating the data noise $\xi(t)$, $\mathbf{c}_{\text{slim}}(t)$ is in error by the vector $\Delta\mathbf{c}_{\text{slim}}(t)$. Then we have

$$\mathbf{G}[\mathbf{c}_{\text{slim}}(t) + \Delta\mathbf{c}_{\text{slim}}(t)] = \mathbf{s}(t) + \boldsymbol{\xi}(t). \tag{10}$$

The SLIM compartmental spectroscopic signal becomes

$$\hat{\mathbf{c}}_{\text{slim}}(t) = \mathbf{c}_{\text{slim}}(t) + \mathbf{G}^{+}\boldsymbol{\xi}(t). \tag{11}$$

The key effects of the noise term are summarized below[6]:

- $\Delta\mathbf{c}_{\text{slim}}(t) = \mathbf{G}^{+}\boldsymbol{\xi}(t)$ is independent of the underlying spectral distribution $\mathbf{c}_{\text{slim}}(t)$, and will not cause systematic intercompartmental spectral leakage.
- Different compartments have different noise sensitivity. Specifically,

$$\Delta c_{\text{slim},m}(t) = \sum_{n=1}^{N} g_{mn}^{+}\xi_n(t) \tag{12}$$

and the variance of $\Delta c_{\text{slim},m}(t)$ is

$$\text{Var}\{\Delta c_{\text{slim},m}(t)\} = \sum_{n=1}^{N} |g_{mn}^{+}|^2\sigma^2 = \|\mathbf{g}_m^{+}\|^2\sigma^2, \tag{13}$$

where $\sigma = \sqrt{\text{Var}\{\xi_n(t)\}}$ and $\mathbf{g}_m^{+} = (g_{m1}^{+}, \ldots, g_{mN}^{+})$ is the mth row vector of the pseudo-inverse matrix $\mathbf{G}^{+}$. It can be justified that $\|\mathbf{g}_m^{+}\| \propto 1/\sqrt{V_m}$ and, thus, the larger a compartment, the lower is its noise sensitivity.[6] For a given set of phase-encoded measurements, the Fourier transform method gives the lowest noise sensitivity. The error of a Fourier reconstruction caused by data noise is given by

$$\Delta c_{\text{ft},m}(t) = \frac{1}{V_m}\int_{\mathcal{D}_m}\sum_{n=1}^{N}\xi_n(t)\text{e}^{i2\pi\mathbf{k}_n\cdot\mathbf{r}}d\mathbf{r}. \tag{14}$$

It can be shown that

$$\sqrt{\frac{\text{Var}\{\Delta c_{\text{slim},m}(t)\}}{\text{Var}\{\Delta c_{\text{ft},m}(t)\}}} = \frac{V_m\|\mathbf{g}_m^{+}\|}{\|\mathbf{g}_m^{*}\|}, \tag{15}$$

which quickly approaches 1 as $\mathbf{G}$ becomes stable.[6]

Effects of Compartmental Inhomogeneities

Compartmental inhomogeneities arise in the SLIM model when any compartments are inaccurately defined, such as the case when several noninteresting compartments are lumped together, and/or when there exist magnetic field inhomogeneities or metabolic inhomogeneities not revealed by the anatomical images. The effects of compartmental inhomogeneities on SLIM are thoroughly examined in Ref. 6. The main results are summarized as follows:

- It is proved that

$$\lim_{N\to\infty}\hat{\rho}_m(f) = \rho_m(f), \tag{16}$$

  which indicates that the SLIM solutions are asymptotically *unbiased* no matter what compartmental inhomogeneities exist!
- For a finite N, SLIM spectra may contain intercompartmental spectral leakage. It is known that,[6] (i) no spectral leakage will come from any homogeneous compartments; (ii) for any inhomogeneous compartment, the constant component will not cause any spectral leakage; and (iii) leakage from higher order inhomogeneities with spatial frequencies well above the highest phase-encoding wave number will be negligible, which implies that heterogeneities in a biological system found at 'microscopic' levels will not be a problem for SLIM, but unmodeled (undiscovered) low-frequency inhomogeneities, such as magnetic field inhomogeneities, would.

Discussion

Equation (5) indicates that, if the encoding vectors are nontrivially chosen, the SLIM spectral function $\hat{\rho}(f)$ can be obtained exactly, provided the number of encodings, N, is not less than the number of compartments, M. Therefore, SLIM can provide exact spatial localization with the minimal number of phase-encodings when the homogeneous compartment model holds. When compartmental inhomogeneities exist, the optimal efficiency of SLIM is lost, namely, one needs to use more encodings than the number of compartments defined to secure a reliable

© 2015 John Wiley & Sons, Ltd.

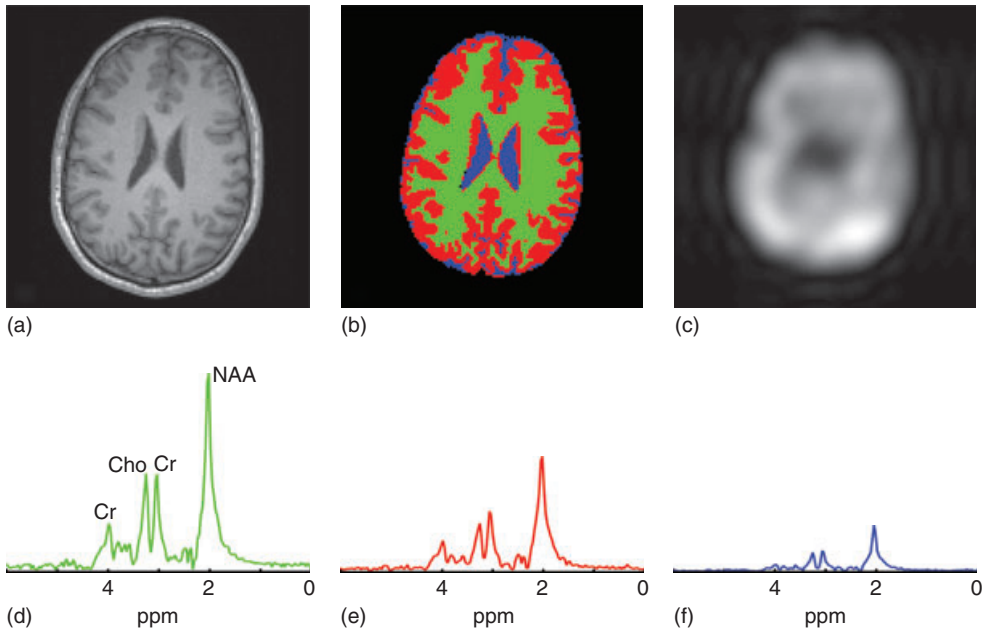

Figure 3. SLIM reconstruction from an in vivo dataset. (a) Anatomical reference image. (b) Supports of the white matter (green), gray matter (red), and CSF (blue) derived from (a). (c) Zero-padded NAA map from a CSI dataset with 12 × 12 spatial encodings. (d–f) Averaged spectrum of the white matter, gray matter, and CSF, respectively, obtained by SLIM

solution. It is found that the number of phase-encoding steps required to stabilize **G** is much less than what is needed by the Fourier method for achieving a comparable localization accuracy (spatial resolution).[6]

Many methods have been proposed to extend SLIM, including Spectral LOcalization with Optimal Pointspread function (SLOOP),[7] Generalized Spectral Localization by IMaging (GSLIM),[8] B_0 compensated Spectral Localization by IMaging (BSLIM),[9] STAtic and Radiofrequency-compensated Spectral Localization by IMaging (starSLIM),[10] SPectral Localization Achieved by Sensitivity Heterogeneity (SPLASH),[11] and Spectroscopy with Linear Algebraic Modeling (SLAM).[12,13] SLOOP optimizes phase encoding gradients to maximize SNR and minimize leakages from heterogeneous compartments (see ***SLOOP and its Modifications***). GSLIM uses a more general signal model to reveal compartmental inhomogeneities and thus reduces leakages from heterogeneous compartments. BSLIM compensates the B_0 field inhomogeneity effects using measured B_0 field inhomogeneity maps, and starSLIM further compensates transmit coil sensitivity (B_1^+) inhomogeneity effects. SPLASH combines SLIM and sensitivity encoding (SENSE[14]) to further reduce the required number of phase encodings. SLAM is one of the most recent extensions of SLIM, which is developed to obtain compartmental averaged spectra using a greatly reduced phase-encoding gradient set (see ***Accelerated Spatially Encoded Spectroscopy of Arbitrarily Shaped Compartments Using Prior Knowledge and Linear Algebraic Modeling***).

Figure 3 shows a set of SLIM reconstruction results using an in vivo dataset collected on a 3T scanner. In this example, SLIM was used to estimate the averaged spectrum of the white matter, gray matter, and cerebrospinal fluid (CSF) of the brain from a CSI dataset with 12 × 12 spatial encodings. The support for the white matter, gray matter, and CSF (Figure 3b) were derived from a high-resolution reference image (Figure 3a) and were then used in the SLIM reconstruction. Directly performing a Fourier transform of the CSI data resulted in a blurred reconstruction, as shown in the NAA concentration map in Figure 3(c), which was zero-padded to a 32 × 32 grid followed by filtering using a Hamming window. Figure 3(d–f) show the averaged spectra of the white matter, gray matter, and CSF, respectively, obtained by the SLIM method.

SPICE: High-resolution MRSI with Subspace Constraints

SPICE[5] is a relatively new approach to using prior knowledge to improve MRSI data acquisition and image reconstruction. As distinct from SLIM, SPICE aims to obtain high-resolution spatiospectral distributions of the imaging object from sparsely sampled data. To this end, it exploits a unique property known as partial separability (PS) of spectroscopic signals.[15,16] This property implies that high-dimensional spectroscopic signals reside in a very low-dimensional subspace and enables special data acquisition and image reconstruction strategies to be used to obtain high-resolution spatiospectral distributions with good SNR. The subspace model, data acquisition schemes, and image reconstruction algorithms for SPICE will be described in the following sections.

Subspace Modeling

SPICE expresses $\tilde{\rho}(\mathbf{r}, t)$ in equation (1) as[5]

$$\tilde{\rho}(\mathbf{r}, t) = \sum_{l=1}^{L} u_l(\mathbf{r}) v_l(t), \tag{17}$$

© 2015 John Wiley & Sons, Ltd.

where $\{v_l(t)\}_{l=1}^{L}$ can be viewed as a set of temporal basis functions, $\{u_l(\mathbf{r})\}_{l=1}^{L}$ are the corresponding spatial coefficients (or viewed as a set of spatial basis functions), and L is the model order (also called the separation rank[15]). In spectroscopic imaging, this PS representation can be justified from different aspects, e.g., the object being imaged has only a finite (L) number of tissue types, each of which has a distinct spectral structure, or it has only a finite number (L) of spectral components. It can be shown that the PS model implies a low separation rank.[15] More specifically, given any point set $\{(\mathbf{r}_m, t_n)\}_{m,n=1}^{M,N}$, the Casorati matrix formed from $\{\tilde{\rho}(\mathbf{r}_m, t_n)\}_{m,n=1}^{M,N}$

$$\mathbf{C}\left(\{\tilde{\rho}(\mathbf{r}_m, t_n)\}_{m,n=1}^{M,N}\right) = \begin{bmatrix} \tilde{\rho}(\mathbf{r}_1, t_1) & \tilde{\rho}(\mathbf{r}_1, t_2) & \cdots & \tilde{\rho}(\mathbf{r}_1, t_N) \\ \tilde{\rho}(\mathbf{r}_2, t_1) & \tilde{\rho}(\mathbf{r}_2, t_2) & \cdots & \tilde{\rho}(\mathbf{r}_2, t_N) \\ \vdots & \vdots & \ddots & \vdots \\ \tilde{\rho}(\mathbf{r}_M, t_1) & \tilde{\rho}(\mathbf{r}_M, t_2) & \cdots & \tilde{\rho}(\mathbf{r}_M, t_N) \end{bmatrix} \quad (18)$$

has a rank upper-bounded by L. Assuming that $\tilde{\rho}(\mathbf{r}, t)$ can be completely specified by $\{\tilde{\rho}(\mathbf{r}_m, t_n)\}_{m,n=1}^{M,N}$ in the conventional pixel representation, the PS or low-rank model implies that $\{\tilde{\rho}(\mathbf{r}_m, t_n)\}_{m,n=1}^{M,N}$ actually resides in a very low-dimensional subspace (i.e., spanned by $\{v_l(t_n)\}_{l,n=1}^{L,N}$) as opposed to the original $M \times N$-dimensional space. Therefore, the PS property significantly reduces the number of degrees of freedom of $\tilde{\rho}(\mathbf{r}, t)$ and, thus, enables special data acquisition and image reconstruction schemes for accelerated high-resolution MRSI, which are described in the next section.

Data Acquisition

SPICE uses a special data acquisition strategy to achieve extended (k, t)-space coverage with sparse sampling. More specifically, it acquires two complementary datasets (called $\mathcal{S}_1$ and $\mathcal{S}_2$), with $\mathcal{S}_1$ covering limited k-space but at a high temporal sampling rate and $\mathcal{S}_2$ covering extended k-space but with limited temporal sampling. $\mathcal{S}_1$ is often called training data as it is used for training the PS model (or determining its temporal basis); $\mathcal{S}_2$ contains the imaging data used to determine the spatial distributions of metabolites (or the spatial coefficients of the PS model). As a result, the SPICE sequence samples (k, t)-space only sparsely, thus reducing data acquisition time.

With the PS model, SPICE offers a range of flexibility for acquiring $\mathcal{S}_1$ and $\mathcal{S}_2$. Illustrative sequences and the resultant sampling trajectories for acquiring $\mathcal{S}_1$ and $\mathcal{S}_2$ are shown in Figures 4 and 5, respectively. For instance, the CSI sequence (Figure 4a) is often used to generate $\mathcal{S}_1$ (assuming good SNR). However, it can also be replaced by a traditional EPSI scheme (Figure 4b) if further improvement in data acquisition speed is desired (e.g., in the case of 3-D SPICE). Many fast acquisition sequences can be used to generate $\mathcal{S}_2$. For example, in the sequence in Figure 5(a), SPICE encodes two spatial dimensions during the FID (in contrast to traditional EPSI sequences that usually encode one spatial dimension) and uses echo shifting (of different excitations) for additional spectral encodings. Alternative sampling trajectories to acquire $\mathcal{S}_2$ include spiral trajectories as shown in Figure 5(b).

Image Reconstruction

Assuming $\mathcal{S}_1 = \{s_1(\mathbf{k}_m, t_n)\}_{m,n=1}^{M_1,N_1}$ and $\mathcal{S}_2 = \{s_2(\hat{\mathbf{k}}_m, \hat{t}_n)\}_{m,n=1}^{M_2,N_2}$, it is understood that: (i) $\{t_n\}_{n=1}^{N_1}$ sample the FID period in high resolution while $\{\hat{t}_n\}_{n=1}^{N_2}$ sample the FID period sparsely and (ii) $\{\mathbf{k}_m\}_{m=1}^{M_1}$ cover only a limited portion of k-space while $\{\hat{\mathbf{k}}_m\}_{m=1}^{M_2}$ cover the entire desired region of k-space (to provide the desired spatial resolution). With these two complementary datasets, SPICE reconstructs $\tilde{\rho}(\mathbf{r}, t)$ using a two-step method: (i) determination of the temporal basis from $\mathcal{S}_1$ and (ii) determination of the spatial coefficients from $\mathcal{S}_2$, while more sophisticated joint estimation schemes can also be used.

If the B_0 field inhomogeneity $\Delta B_0(\mathbf{r})$ is negligible, estimation of the temporal basis (or temporal subspace), $\{v_l(t_n)\}_{l=1}^{L}$ for $n = 1, 2, \ldots, N_1$, from $\mathcal{S}_1$ is fairly easy. For instance, a set of $\{v_l(t_n)\}_{l,n=1}^{L,N_1}$ can be obtained by performing a singular value decomposition (SVD) of the Casorati matrix formed from $\{s_1(\mathbf{k}_m, t_n)\}_{m,n=1}^{M_1,N_1}$. However, $\Delta B_0(\mathbf{r})$ can be very significant in practical experiments. Therefore, we need to first remove or reduce its effects on $\mathcal{S}_1$ for accurate subspace estimation. The challenge specific to this problem is the limited k-space coverage for $\mathcal{S}_1$. To address this challenge, we correct the field inhomogeneity by performing the following regularized reconstruction:

$$\hat{\boldsymbol{\rho}} = \arg \min_{\boldsymbol{\rho}} \|\mathbf{s}_1 - \Omega_1 \mathcal{F}_B\{\boldsymbol{\rho}\}\|_2^2 + \lambda_1 R(\boldsymbol{\rho}), \quad (19)$$

where the $\|\cdot\|_2^2$ term measures the data consistency of a reconstruction; $R(\cdot)$ is a regularization functional with regularization parameter λ_1; $\hat{\boldsymbol{\rho}}$, a field corrected reconstruction; $\mathbf{s}_1$, a vector containing data from $\mathcal{S}_1$; Ω_1, a sampling operator for the limited k-space coverage for $\mathcal{S}_1$; and $\mathcal{F}_B$, a Fourier encoding operator including the B_0 field inhomogeneity effects described in equation (1). Different regularization terms can be used for $R(\cdot)$ to incorporate prior information about $\boldsymbol{\rho}$, e.g., in the form of a weighted-ℓ_2 norm using prior structural information from anatomical imaging.[17,18] Note that for the field correction scheme in equation (19), we assume that an accurate $\Delta B_0(\mathbf{r})$ map can be acquired during the MRSI experiment. After correction, a set of corrected data, denoted as $\{\hat{s}_1(\mathbf{k}_m, t_n)\}_{m,n=1}^{M_1,N_1}$, is then generated from $\hat{\boldsymbol{\rho}}$ and used to form an $M_1 \times N_1$ Casorati matrix $\mathbf{C}(\{\hat{s}_1(\mathbf{k}_m, t_n)\}_{m,n=1}^{M_1,N_1})$ as in equation (18). The SVD is then applied to this matrix and its L principal right singular vectors are chosen as the estimated temporal basis, denoted as $\{\hat{v}_l(t_n)\}_{l,n=1}^{L,N_1}$.

With the temporal basis determined, the spatial coefficients, $\{u_l(\mathbf{r}_m)\}_{l=1}^{L}$, can be estimated from the sparse data in $\mathcal{S}_2$ by solving a regularized least-squares problem. For simplicity, assuming $N = N_1$ and $M = M_2$, we rewrite $\{\tilde{\rho}(\mathbf{r}_m, t_n)\}_{m,n=1}^{M,N} = \{\sum_{l=1}^{L} u_l(\mathbf{r}_m)\hat{v}_l(t_n)\}_{m,n=1}^{M,N}$ as $\mathbf{U}\hat{\mathbf{V}}$ (with $\mathbf{U} \in \mathbb{C}^{M\times L}$ and $\hat{\mathbf{V}} \in \mathbb{C}^{L\times N}$ being two rank-L matrices such that $\mathbf{U}_{ml} = u_l(\mathbf{r}_m)$ and $\hat{\mathbf{V}}_{\ln} = \hat{v}_l(t_n)$). Accordingly, the spatial coefficients can be determined by solving

$$\hat{\mathbf{U}} = \arg \min_{\mathbf{U}} \|\mathbf{s}_2 - \Omega_2 \mathcal{F}_B\{\mathbf{U}\hat{\mathbf{V}}\}\|_2^2 + \lambda_2 \Psi(\mathbf{U}, \hat{\mathbf{V}}), \quad (20)$$

where $\mathbf{s}_2$ denotes the vector containing all the data in $\mathcal{S}_2$, $\mathcal{F}_B$ represents the Fourier encoding operator as in equation (19), Ω_2 represents the (k, t)-space sampling operation used for

© 2015 John Wiley & Sons, Ltd.

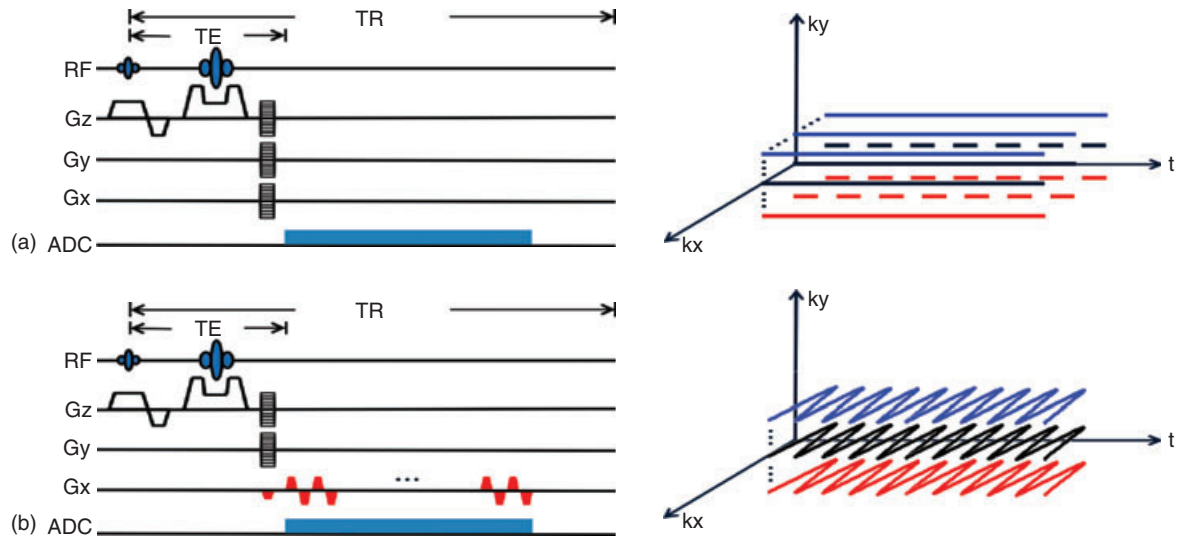

Figure 4. Two example sequences for acquiring $\mathcal{S}_1$. (a) A CSI sequence and the resultant sampling trajectory. (b) An EPSI sequence and the resultant sampling trajectory

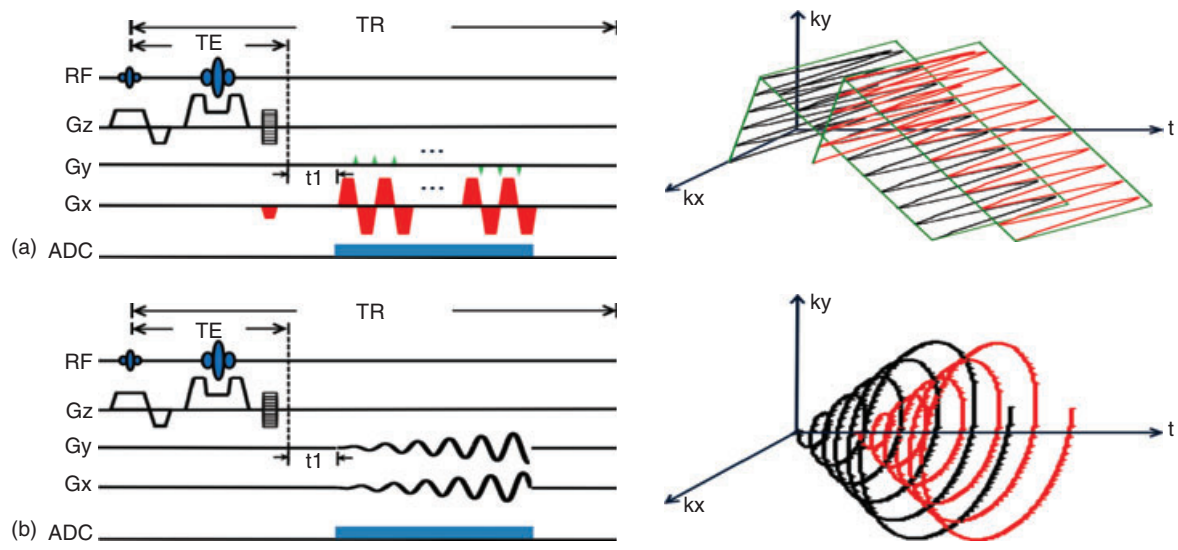

Figure 5. Two example sequences for acquiring $\mathcal{S}_2$. Two spatial directions are encoded simultaneously during each FID (along with spectral encoding) using (a) an EPI-like trajectory or (b) a spiral trajectory. Additional spectral encodings are obtained through echo shifting (separated by t1 as shown in the sequence diagrams)

acquiring $\mathcal{S}_2$, and $\Psi(\cdot)$ is a regularization functional with parameter λ_2. There are many choices for $\Psi(\cdot)$ to incorporate prior information about $\tilde{\rho}(\mathbf{r},t)$ or $\rho(\mathbf{r},f)$ (including both quadratic and sparsity-promoting penalties[18–21]). For instance, $\Psi(\mathbf{U},\hat{\mathbf{V}}) = \|\mathbf{WDU}\hat{\mathbf{V}}\|_F^2$, where $\mathbf{D}$ is a finite difference operator and $\mathbf{W}$ contains edge weights derived from high-resolution anatomical images.[18] Integrating this ℓ_2-regularization term into equation (20) yields a problem equivalent to solving a system of linear equations that can be done efficiently using various algorithms, such as the linear conjugate gradient method.[22] The entire processing pipeline for SPICE is summarized in the flow chart in Figure 6.

Discussion

The spectral bandwidth and spatial resolution of a SPICE reconstruction can be characterized by analyzing the spectral property of the temporal basis and the resolution property of the spatial coefficients, respectively. The spectral bandwidth of the temporal basis is determined by the temporal sampling rate of $\mathcal{S}_1$, while the resolution of the spatial coefficients is determined by the k-space coverage of $\mathcal{S}_2$. In practice, spatial regularizations are often used for improved spatial coefficient estimation. If a weighted-ℓ_2 regularization is used in equation (20), the resultant linear spatiospectral reconstruction

© 2015 John Wiley & Sons, Ltd.

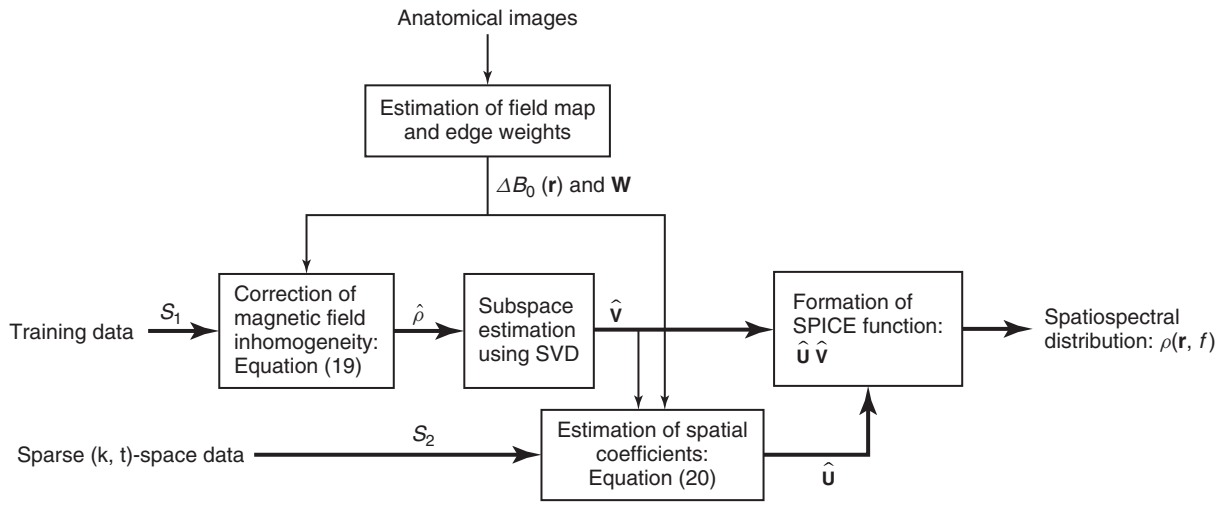

Figure 6. SPICE processing flow chart

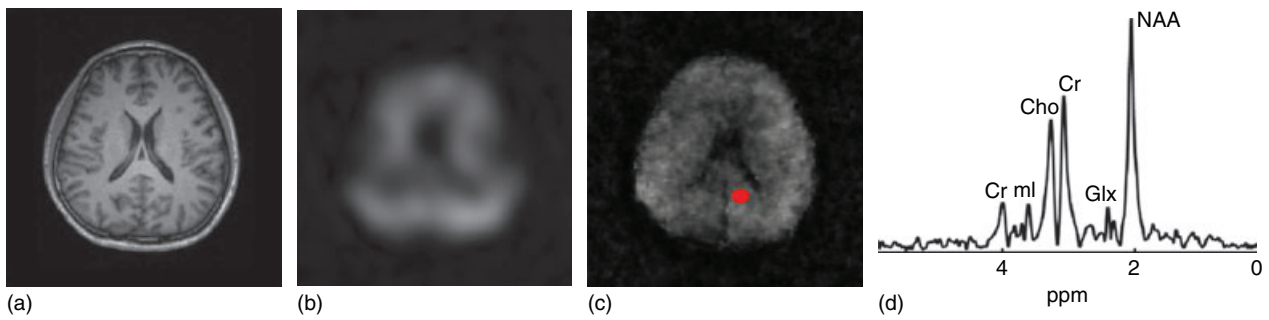

Figure 7. SPICE reconstruction from an in vivo dataset. (a) Anatomical image. (b) NAA map obtained by the conventional CSI method (24 × 24 spatial encodings, 9.2 mm in-plane resolution, 15.3 min scan). (c) NAA map obtained by SPICE (112 × 112 spatial encodings, 2.0 mm in-plane resolution, 15.7 min scan). (d) A representative spectrum from the marked pixel. The labeled peaks are due to NAA, Cr, Cho, glutamate/glutamine (Glx), and myo-inositol (mI)

can be expressed as $\hat{\rho}(\mathbf{r},f) = \int \rho(\mathbf{r}',f)h(\mathbf{r},\mathbf{r}')d\mathbf{r}'$, where $\rho(\mathbf{r},f)$ is the true spatiospectral function and $h(\mathbf{r},\mathbf{r}')$ is the so-called spatial response function (SRF)[18] (which can be spatially varying). Accordingly, the resolution property of $\hat{\rho}(\mathbf{r},f)$ can be characterized by analyzing $h(\mathbf{r},\mathbf{r}')$. If an ℓ_1 regularization is used, the resolution analysis is much more difficult owing to the nonlinear reconstruction process. However, it is possible to construct locally quadratic approximations for calculating a series of local response functions to analyze resolution, which would be interesting to pursue in future research.

The SNR of SPICE reconstructions can be characterized by analyzing the noise properties of the estimated temporal basis and spatial coefficients. With a properly chosen model order, the power of the noise in the estimated temporal basis is determined by the noise in $\mathcal{S}_1$, which can be easily characterized based on SVD. The power of the noise in the estimated spatial coefficients is determined by the noise in $\mathcal{S}_2$, which can be characterized using standard variance analysis if the spatial coefficients are determined by solving a least-squares problem as in equation (20). In general, $\mathcal{S}_2$ is collected in a rapid scan with significantly higher readout bandwidths, therefore the effects of the noise in $\mathcal{S}_2$ are often dominant in the final SPICE reconstructions.

For ^{1}H spectroscopic imaging, suppression or removal of the nuisance signals (water and lipid signals) is necessary, which has been well studied for CSI and EPSI acquisitions.[23–26] SPICE samples (k,t)-space sparsely for efficient spatiospectral encoding, thus, specialized nuisance signal suppression or removal methods need to be developed. We have developed a nuisance signal removal method to address this issue using a novel union-of-subspaces model.[27] Our method exploits the PS properties of both the nuisance and the metabolite signals and has enabled accurate estimation and effective removal of the nuisance signals from ^{1}H-MRSI data of the brain that have limited and/or sparse (k,t)-space coverage.

Figure 7 shows a set of SPICE reconstruction results from an in vivo dataset collected on a 3T scanner. The SPICE acquisition was 15.7 min, including a 3.8 min CSI acquisition with 12 × 12 spatial encodings and a 11.9 min EPSI acquisition with 112 × 112 spatial encodings (2.0 mm nominal in-plane resolution) averaged four times. The rest of the imaging parameters were 10 mm slice thickness, 220 mm × 220 mm FOV, 1600/30 ms TR/TE, 2000 Hz readout bandwidth for the

© 2015 John Wiley & Sons, Ltd.

CSI scan, and 100 kHz readout bandwidth for the EPSI scan. Water suppression enhanced through T_1 effects (WET) pulses[23] were used for water suppression and outer-volume-suppression pulses were used for lipid suppression. For comparison, another CSI dataset was collected in roughly the same acquisition time with 24 × 24 spatial encodings (9.2 mm nominal in-plane resolution) and the corresponding results were obtained using a conjugate phase reconstruction.[28] As can been seen, the NAA map obtained by the conventional CSI method (Figure 7b) has significant blurring artifacts, while SPICE achieved both high-spatial resolution and good SNR as shown by the NAA map (Figure 7c) and the representative spectrum (Figure 7d).

Acknowledgments

The work was supported in part by the following research grants: NIH-P41-EB015904, NIH-P41-EB001977, NIH-1RO1-EB013695, and Beckman Postdoctoral Fellowship (to Chao Ma).

Biographical Sketches

Chao Ma. *b* in 1982. BS, 2004, Tsinghua University; MS, 2007, Tsinghua University; PhD, 2013, University of Illinois at Urbana-Champaign. He is currently a Beckman postdoctoral fellow at the University of Illinois at Urbana-Champaign. Research interests include RF pulse design, image reconstruction, and spectroscopic imaging.

Fan Lam. *b* in 1985. BS, 2008, Tsinghua University; MS, 2011, University of Illinois at Urbana-Champaign. He is currently a PhD candidate in the Department of Electrical and Computer Engineering at the University of Illinois at Urbana-Champaign. Research interests include sparse sampling, denoising and parameter estimation, and spectroscopic imaging.

Zhi-Pei Liang. *b* in 1961. BS, 1982, South-China University of Technology; PhD, 1989, Case Western Reserve University; Research Associate under Paul Lauterbur, 1989–1991. He is currently Franklin W. Woeltge Professor of Electrical and Computer Engineering at the University of Illinois at Urbana-Champaign. Research interests include spin dynamics and image formation theory, algorithms, and biomedical applications.

Related Articles

Development of NMR: Biological and Medical MR Spectroscopy; Chemical Shift Imaging; CSI and SENSE CSI; SLOOP and its Modifications; Accelerated Spatially Encoded Spectroscopy of Arbitrarily Shaped Compartments Using Prior Knowledge and Linear Algebraic Modeling; High-speed MRS with PEPSI and spiral MRS.

References

1. T. R. Brown, B. M. Kincaid, and K. Ugurbil, *Proc. Natl. Acad. Sci. U.S.A.*, 1982, **79**, 3523.
2. R. Pohmann, M. von Kienlin, and A. Haase, *J. Magn. Reson.*, 1997, **129**, 145.
3. S. Posse, G. Tedeschi, R. Risinger, R. Ogg, and D. Le Bihan, *Magn. Reson. Med.*, 1995, **33**, 34.
4. X. Hu, D. N. Levin, P. C. Lauterbur, and T. Spraggins, *Magn. Reson. Med.*, 1988, **8**, 314.
5. F. Lam and Z.-P. Liang, *Magn. Reson. Med.*, 2014, **71**, 1349.
6. Z.-P. Liang and P. C. Lauterbur, *J. Magn. Reson., Ser. B*, 1993, **102**, 54.
7. M. von Kienlin and R. Mejia, *J. Magn. Reson.*, 1991, **94**, 268.
8. Z.-P. Liang and P. C. Lauterbur, *IEEE Trans. Med. Imaging*, 1991, **10**, 132.
9. I. Khalidov, D. Van De Ville, M. Jacob, F. Lazeyras, and M. Unser, *IEEE Trans. Med. Imaging*, 2007, **26**, 990.
10. A. Passeri, S. Mazzuca, and V. Del Bene, *Phys. Med. Biol.*, 2014, **59**, 2913.
11. L. An, S. Warach, and J. Shen, *Magn. Reson. Med.*, 2011, **66**, 1.
12. Y. Zhang, R. E. Gabr, M. Schar, R. G. Weiss, and P. A. Bottomley, *J. Magn. Reson.*, 2012, **218**, 66.
13. Y. Zhang, R. E. Gabr, J. Zhou, R. G. Weiss, and P. A. Bottomley, *J. Magn. Reson.*, 2013, **237**, 125.
14. K. P. Pruessmann, M. Weiger, M. B. Scheidegger, and P. Boesiger, *Magn. Reson. Med.*, 1999, **42**, 952.
15. Z.-P. Liang, In *Proceeding of IEEE International Symposium on Biomedical Imaging, Arlington*, 2007, 988.
16. J. P. Haldar and Z.-P. Liang, In *Proceeding of IEEE International Symposium on Biomedical Imaging, Rotterdam*, 2010, 716.
17. X. Peng, H. Nguyen, J. P. Haldar, D. Hernando, X. P. Wang, and Z.-P. Liang, In *Proceeding of Annual International Conference of the IEEE Engineering in Medicine and Biology Society, Buenos Aires*, 2010, 883.
18. J. P. Haldar, D. Hernando, S. K. Song, and Z.-P. Liang, *Magn. Reson. Med.*, 2008, **59**, 810.
19. J. Kornak, K. Young, B. J. Soher, and A. A. Maudsley, *IEEE Trans. Med. Imaging*, 2010, **29**, 1333.
20. R. Eslami and M. Jacob, *IEEE Trans. Med. Imaging*, 2010, **29**, 1297.
21. J. Kasten, F. Lazeyras, and D. Van De Ville, *IEEE Trans. Med. Imaging*, 2013, **32**, 1853.
22. G. H. Golub and C. F. VanLoan, 'Matrix Computation', Johns Hopkins University Press: Baltimore, 1983.
23. R. J. Ogg, P. B. Kingsley, and J. S. Taylor, *J. Magn. Reson., Ser. B*, 1994, **104**, 1.
24. J. H. Duyn, J. Gillen, G. Sobering, P. C. M. van Zijl, and C. T. W. Moonen, *Radiology*, 1993, **188**, 277.
25. C. I. Haupt, N. Schuff, M. W. Weiner, and A. A. Maudsley, *Magn. Reson. Med.*, 1996, **35**, 678.
26. G. Metzger, S. Sarkar, X. Zhang, K. Heberlein, M. Patel, and X. Hu, *Magn. Reson. Imaging*, 1999, **17**, 435.
27. C. Ma, F. Lam, C. L. Johnson, and Z.-P. Liang, *Magn. Reson. Med.*, in press .
28. D. C. Noll, J. A. Fessler, and B. P. Sutton, *IEEE Trans. Med. Imaging*, 2005, **24**, 325.

© 2015 John Wiley & Sons, Ltd.